

# Distribution of SLS Integrated Load Uncertainty to Surface Pressures and Sectional Loads

Derek J. Dalle\*, Stuart E. Rogers\*,  
Aaron C. Burkhead\*, Jamie G. Meeroff\*  
Corresponding author: [derek.j.dalle@nasa.gov](mailto:derek.j.dalle@nasa.gov)

\* NASA Ames Research Center, Computational Aerosciences Branch

**Abstract:** Aerodynamic loads that are important to launch vehicle programs such as NASA’s Space Launch System (SLS) include both integrated loads such as the force & moment on the entire vehicle and distributed loads. In this work two examples of distributed loads are considered: the pressure field on the surface of the vehicle and sectional loads, which are one-dimensional distributions along the axis of the launch vehicle. In some modern flight programs, the integrated loads, such as lift and drag, used to design the guidance and control laws for the vehicle come from wind tunnel testing, while distributed loads are produced using Computational Fluid Dynamics (CFD). The first task that is addressed in this paper, then, is to provide a formal method to adjust the distributed loads so that integrating them matches the prescribed integrated load. In addition, the integrated loads in a launch vehicle typically include an uncertainty estimate. The second task is to distribute this prescribed integrated uncertainty to each point in a distributed load. Both tasks are addressed using the same technique, which is to create distributed load profiles that isolate adjustments to one integrated load while leaving the others unaffected. These adjustments are informed by Proper Orthogonal Decomposition (POD) of the entire CFD-based distributed load database. Once applied, the adjusted distributed loads can be used to evaluate any scalar quantity of interest that might be needed by downstream users such as structural analysis or trajectory modelers.

*Keywords:* Computational Fluid Dynamics, Launch Vehicles, Uncertainty Quantification, Proper Orthogonal Decomposition

## 1 Introduction

The Space Launch System (SLS) is a super heavy-lift launch vehicle under development at the National Aeronautics and Space Agency (NASA) and its contractors [1], that has the capability of sending humans beyond Earth orbit for the first time in almost 50 years [2]. Together with the Orion spacecraft [3], Exploration Ground Systems (EGS) [4], Gateway [5], Human Landing System, and other programs, SLS is a key part of NASA’s Artemis program that will return humans, including the first woman and the first person of color, to the Moon for the first time since Apollo. An image of SLS, Orion, and some of the EGS ground systems for the Artemis I mission is shown in Figure 1.

Because the operator of these programs and missions, NASA, is a public agency, new engineering techniques and results are often published, benefiting the public in general and the aerospace industry in particular. In addition, executing such a large enterprise within NASA provides practical experience to NASA’s leading aerospace engineers and researchers, which improves the applicability of NASA research to current space industry needs.

This paper focuses on handling of aerodynamic loads across a large launch vehicle program. Aerodynamic loads for a launch vehicle can be estimated using a variety of methods, including wind tunnel experimentation, theoretical models, numerical modeling such as CFD, and flight test. Each of these potential data sources has its own advantages and disadvantages. For a program like SLS, which has not flown yet, the two primary



Figure 1: Artemis I vehicle including SLS, Orion spacecraft, and EGS hardware at Launch Pad 39B on March 18, 2022

data sources are wind tunnel testing and CFD. Some of the key advantages and limitations of these two data sources as they relate to SLS are:

- Each CFD solution has a high spatial density of information and can provide modeling for the entire surface of the vehicle and the flow around it whereas wind tunnel testing is best suited for scalar measurements like total forces & moments or pressures at directly instrumented points.
- CFD can directly model flight hardware and flight conditions, for example including rocket plumes and running at the flight Reynolds number and scale.
- Measurements from wind tunnel testing are typically associated with a higher degree of trust because they are not subject to numerical error and have a long history of applications in launch vehicle programs.

Without going into too much detailed discussion about these concepts, the approach of SLS has generally been to use wind tunnel testing where practical and CFD for all other needed aerodynamic products. In particular this means for SLS that the integrated aerodynamic loads (i.e. the total forces and moments in three axes on the entire vehicle) used by the program are directly from wind tunnel testing [6]. Distributed loads, on the other hand, such as the surface pressure field on the entire surface of the vehicle, are derived from CFD [7]. Because the integrated and distributed loads come from different sources, there are two desirable properties that are not necessarily met:

1. The integral of the distributed loads should match the integrated loads.
2. It should be possible to disperse loads as part of an uncertainty analysis without violating item #1.

SLS is an example of a program where the integral loads and distributed loads are derived from different data sources, and so integrating the nominal distributed loads yields a result different from the official integrated

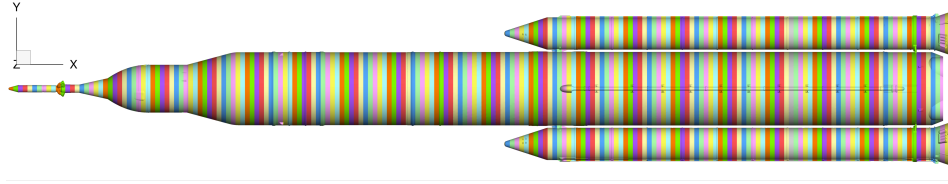


Figure 2: Sectional load slices for SLS Block 1B configuration

loads. For example, integrating  $z$ -component of the force from the surface pressure database does not match the  $C_N$  for the same flight condition. In other words, desired property #1 from above is not satisfied.

Furthermore, each integrated load has an uncertainty estimate, essentially stating that the force or moment can take a range of possible values. Therefore satisfying desired property #2 from above means repeating the same process as for #1, but for many possible values of the forces & moments at each flight condition.

In the SLS program, there are two major types of distributed loads: surface pressures and sectional loads. The surface pressure database contains the pressure coefficient at all points on the vehicle for all expected flight conditions and is relatively simple to understand but contains a large amount of data. The sectional load database is essentially a projection of this database into 1D. This means dividing the vehicle into a number of slices, as shown in Figure 2, and calculating the load on each slice.

For the SLS program, both the surface pressures and the sectional loads are derived from the same CFD simulations, so they are consistent except that the sectional loads include viscous forces while the surface pressure database does not.

In order to satisfy the two consistency constraints mentioned above, this paper develops a method based on Proper Orthogonal Decomposition [8] of the surface pressure database that creates adjustments to the distributed loads such that they are consistent with externally defined integral loads. A similar adjustment to distributed loads that adjusts only the sectional loads was discussed in [9]. This work extends the ideas from [9] by applying them directly to the surface pressures and is similar to the approach in [10] used for sectional loads in the liftoff & transition phase of SLS flight (the present work focuses on the ascent phase that follows liftoff & transition).

The advantages of applying the adjustments directly to the surface pressures are:

- Adjusted line loads can still be acquired as a surface pressure leads directly to a sectional load.
- Adjusting the surface pressure allows for cross-correlation, in which for example the vertical component of line loads may change due to a dispersion in integrated axial force.
- Adjustments are consistent with all six integrated forces & moments simultaneously.
- Having a consistent surface pressure distribution means many other engineering analyses can use dispersed and consistent aerodynamic environments.

The result of the technique developed here is the creation of a surface pressure profile for each integrated load. So for example there is a surface pressure distribution that adjusts the integrated force coefficient in the axial direction,  $C_A$ , by +1 at Mach 1.75 while leaving the force in the other perpendicular directions, along with all the moments, unchanged. This approach is developed with the goal of maximum simplicity for down-stream users such as structural engineers and guidance, navigation, & control teams.

For the phase of SLS flight known to the aerodynamics team as “ascent”, which lasts from about 30 seconds into the flight to 2 minutes (more precisely when the vehicle reaches Mach 0.5 up to booster separation), the NASA Ames SLS CFD Team runs approximately 1000 separate simulations in order to provide information about all possible flight conditions. For Artemis I, this analysis has been conducted at least four times (along with more limited analysis sets from the early phases of the program) using FUN3D [11] and OVERFLOW [12] both with and without plume models for the four RS-25 engines on the SLS core stage and two Solid Rocket Booster (SRB, hereinafter usually just “booster”) motors. More details about how these CFD solutions are obtained are provided in Section 2.

Table 1: Number of CFD solutions available from each Block 1 ascent database

Solver	Plume	Num. Solutions
FUN3D 13.1	power-off	1131
FUN3D 13.1	power-on	1380
OVERFLOW 2.2L	power-off	907
OVERFLOW 2.2L	power-on	6

Those 1000 or so CFD solutions are divided into an approximately fixed set of angle of attack ( $\alpha$ ) and sideslip angle ( $\beta$ ) combinations at preselected Mach numbers ( $M$ ) from 0.5 to 5.0. Because so many CFD solutions are readily available at each Mach number, the POD-based technique discussed in this paper does not require any additional CFD solutions. Instead the information already in the database about how angle of attack and sideslip angle affect the surface pressure are used to create representative surface pressure modes. Section 3 describes step-by-step how these adjustment modes are created and includes more details about the CFD surface pressure database (Section 3.1) and some images of sample POD modes (Section 3.2). Using SLS an example, Section 4 shows sample results of adjusted distributed loads and sample implications for sectional loads and other products that use distributed aerodynamic loads as input. Finally Section 5 discusses various extensions to the methods presented here, some limitations of the approach, and the relationship of these methods to direct uncertainty quantification of distributed loads as discussed for example in [13].

## 2 CFD Methodology

The results in this paper use a set of CFD solutions produced in 2017 for design certification of the Block 1 configuration of SLS to used for the first three Artemis missions. For that design cycle, the aerodynamics team conducted an extensive verification analysis that include grid convergence analysis, turbulence model sensitivity studies, rocket exhaust plume modeling effects, and code-to-code comparisons. As a result of these investigations, there are three separate full CFD databases of SLS Block 1 ascent, each with at least 900 converged solutions. Two CFD software packages with very different meshing paradigms but otherwise largely overlapping capabilities were used: OVERFLOW 2.2L from NASA Langley Research Center [12] and FUN3D 13.1 also from NASA Langley Research Center [11]. Some of the solutions included simulated plumes for the four RS-25 Core Stage engines and the solid rocket motors on each of two boosters; simulations including the plumes are labeled “power-on,” and those without are labeled “power-off”. All CFD solutions studied here were performed for the Artemis I SLS configuration on the *Pleiades* supercomputers at the NASA Advanced Supercomputing (NAS) facility<sup>1</sup>. Table 2 shows how many CFD solutions have been archived for each permutation of solver and plume model. In the following sections, results from the middle two databases (power-on FUN3D and power-off OVERFLOW) are analyzed and compared to show how two different databases on the same vehicle configuration perform when the distributed load adjustment procedures are applied.

FUN3D is a fully unstructured solver for the 3D Navier-Stokes equations developed at NASA Langley Research Center. For this work, version 13.1 [11] was used, with a modification to write surface output in `.plt` format instead of `.szplt`<sup>2</sup>. The solutions are Reynolds-averaged Navier-Stokes (RANS) solutions with turbulence closure from the one-equation Spalart-Allmaras [14] turbulence model, and the flow is considered turbulent everywhere. Non-slip, cold walls with the default FUN3D temperature were used to model the surface boundaries of the vehicle except for the flow-through faces in the plenums of the six nozzles where simulated fuel and oxidizer enters the flow, which used total pressure and subsonic pressure<sup>3</sup> to set the thrust conditions. The throat and subsonic regions of each nozzle were modified to match thrust and mass flow but not temperature. The simulations used the perfect-gas version of FUN3D, so the exhaust is modeled as high-temperature air and cannot match all three of thrust, mass flow rate, and temperature.

<sup>1</sup>The 2017 simulations used in this work predate the additions of the *Electra* and *Aitken* systems at NAS.

<sup>2</sup>Getting the `.plt` output format requires the `-plt_tecplot_output` option when calling FUN3D’s solver.

<sup>3</sup>This is FUN3D boundary condition 7011.

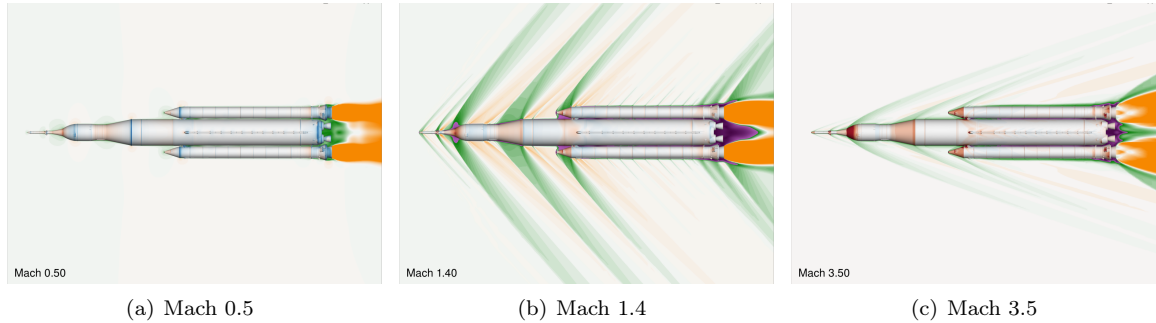


Figure 3: Flow visualization of select FUN3D solutions of Artemis I ascent at zero degrees  $\alpha$  and  $\beta$ . Vehicle surface is colored by pressure contours, where blue is low and red is high. A solution slice through the center plane of the vehicle shows Mach number with green for local Mach less than freestream and orange for higher. Purple is used in the two supersonic solutions to highlight regions of subsonic flow.

Two feature-based mesh adaptation cycles were performed using Mach number as the feature scalar key and the older `delta-1` option. Unstructured meshes with triangular-prism layers cells and mostly tetrahedral volume cells were generated using AFLR3 [15] with a wall spacing ensuring  $y^+ \leq 1$  for the highest-Reynolds number flight condition in the trajectory. The initial mesh had 53 million nodes, and the mesh refinement within FUN3D added another 7 million nodes; the final mesh had a total of 175 million cells. The surface mesh, which was not affected by mesh adaptation, had 950 thousand nodes and 1.9 million triangular faces. Some example flow results are show in Figure 3.

OVERFLOW is a structured-overset grid CFD solver developed at Langley Research Center and has a long history of support for NASA’s missions [12]. The OVERFLOW solutions in this work were performed using version 2.2L, including the Cartesian off-body grid adaptation capability [16]. The initial grid system for these OVERFLOW grids contained 1833 near-body grids and 548 million total points. A unique surface triangulation was created from the full set of surface grids for various post-processing procedures, including creating a surface pressure database with a single unique pressure coefficient for every point on the surface. That surface triangulation was created using `usurp` and contains 6.6 million nodes and 13 million triangles. The adaptation routine was allowed to grow the volume mesh to 600 million total points. From these numbers it is apparent that the OVERFLOW solutions were obtained on a substantially finer grid, which was one of the motivations of the detailed CFD verification study and also makes the comparison of their surface pressure adjustments interesting.

For both solvers, a nominal sequence of steady-state iterations was run; in the FUN3D this ended at 3000 iterations, and for the OVERFLOW runs it was 20000. An additional sequence of unsteady RANS iterations with a non-dimensional time step of 1.0 and 5 subiterations was prepared for cases where deemed necessary. For cases with a Mach number less than or equal to 1.2, the unsteady iterations were automatically executed, while they were only added as judged necessary for other cases after viewing iterative histories of the three major bodies (left booster, right booster, and centerbody) and some major protuberances (i.e. other parts of the vehicle that protrude from the main launch vehicle body). For OVERFLOW the additional iterations required at least 4000 iterations, while for FUN3D it was 1000. Finally, additional unsteady iterations were added as needed until the major iterative histories were judged (by a human) to have reached either a steady state or a limit cycle.

While improvements could and have been made to the various technologies and procedures used to create this data set, it is rare in that the entire database and not just select cases were run using two very different approaches. For a database post-processing procedure such as described in this work, the SLS Block 1 ascent CFD data set is a perfect test subject.

### 3 Adjusting Distributed Loads

Once the distributed loads have been adjusted to match an integrated load, the same approach can be used to adjust them again to match a dispersed integrated load as part of an uncertainty quantification. For example, if the nominal  $C_N$  for a given flight condition is 0.7, the database might say that the real value may be between 0.55 and 0.85. This can be described as a simple equation:

$$\tilde{C}_N = C_N + \varepsilon_{CN} U_{CN} \quad (1)$$

where  $C_N$  is the nominal normal force coefficient,  $\varepsilon_{CN} \in [-1, 1]$  is a random variable that samples a specified probability distribution function,  $U_{CN}$  is the magnitude of uncertainty in  $C_N$ , and  $\tilde{C}_N$  is the dispersed value.

Once the distributed loads have been adjusted to match  $C_N$ , the same approach can be used to adjust them further to match  $\tilde{C}_N$ . Using this approach, each point in the distributed load will have a probability distribution function (PDF) that is proportional (possibly reversed) to the integrated load. For example if  $\varepsilon_{CN}$  is normally distributed, then the surface pressure profiles will be normally distributed at every point on the surface. In general PDFs of local features (such as pressure coefficient) may be bimodal or even more complex, especially in the presence of shocks [13, 17].

In the present work, this known limitation is tolerated because the statistics of the uncertainty estimate, both the PDF of  $\varepsilon_{CN}$  and the scale  $U_{CN}$ , are specified by external models. There is no set of numerical simulations that can be expected to reproduce the target integrated load PDF, especially since that uncertainty estimate may include safety margins and estimates of changes to the geometry between analysis and flight. A technique with limitations still provides value compared to the typical situation in which distributed loads are considered deterministic by engineers who use them for other analysis.

In [9] we discussed a technique to directly adjust the sectional loads (also known as line loads). In this work we extend this work by instead adjusting the surface pressures and then evaluating the line loads from the adjusted surface pressures.

The outline of this approach is as follows:

1. Divide the database of distributed loads into a number of families; for SLS ascent, the families are the cases with the same Mach number.
2. Calculate a Proper Orthogonal Decomposition (POD) of the distributed loads for each family.
3. For each of the 6 integrated load coefficients, find an optimal linear combination of the POD modes that adjust one integrated coefficient without affecting the other 5.

This approach requires a sufficient number CFD solutions in each family to perform the POD [8]. At a minimum there must be at least 6 CFD solutions available for each family since there are 6 constraints, and results will improve with substantially more than this. For the SLS program, we typically have 69 cases for each Mach number, so this adjustment and dispersion method does not require any additional CFD simulations.

#### 3.1 Description of SLS Distributed Load Databases

A flight condition is a unique combination of Mach number ( $M$ ), angle of attack ( $\alpha$ ), and sideslip angle ( $\beta$ ). A typical ascent database consists of solutions at about 19 different Mach numbers and fixed set of about 69 combinations of  $\alpha$  and  $\beta$  for each Mach number. For convenience we use  $\mathbf{r}$  to denote a single flight condition and  $\mathbf{x}$  as a node on the surface grid of the CFD solution

$$\mathbf{r}_i = \begin{bmatrix} M_i \\ \alpha_i \\ \beta_i \end{bmatrix} \quad \mathbf{x}_j = \begin{bmatrix} x_j \\ y_j \\ z_j \end{bmatrix} \quad (2)$$

At each flight condition, the surface pressure coefficient ( $c_p$ ) at each point on the surface grid is saved as

an array. So for flight condition  $\mathbf{r}_i$ , the surface pressure array is

$$\mathbf{c}_i = \begin{bmatrix} c_{p,i,1} \\ c_{p,i,2} \\ \vdots \\ c_{p,i,n_x} \end{bmatrix} \quad (3)$$

where

$$c_{p,i,j} = c_p(\mathbf{r}_i, \mathbf{x}_j) \quad (4)$$

is the surface pressure coefficient at node  $j$  of flight condition  $i$ . For convenience we drop the  $p$  subscript in (3) when writing the array of surface pressure  $\mathbf{c}$ .

The surface pressure database is a large matrix in which each column is one of the surface pressure arrays from above. So for example

$$\mathbf{C}_{db} = [\mathbf{c}_1 \quad \mathbf{c}_2 \quad \cdots \quad \mathbf{c}_{n_r}]$$

where  $n_r$  is the number of CFD solutions (also the number of flight conditions).

### 3.2 Proper Orthogonal Decomposition

In order to anchor the adjustments to the surface pressures to information from the existing CFD solutions and also extract the most meaningful features from the surface pressure database, the use of a Proper Orthogonal Decomposition (POD) approach is considered. The POD approach is closely tied to the Singular Value Decomposition (SVD). POD is a Reduced Order Model (ROM) technique that has been used for many aerospace applications [8, 18, 19]. It is a technique that identifies the primary signal from a large data set in a robust and automated way. This section describes how it can be applied to distributed load analysis using the surface pressure field from one CFD solution as the input ‘‘snapshot’’ and using a family of such solutions and snapshots to identify typical surface pressure shapes.

First divide the pressure into a number of subsets (herein called ‘‘families’’). As described previously, the Mach number is used for this grouping in the present SLS example, so each family consists of CFD solutions computed at the same flight Mach number. So if  $k_1, k_2, \dots, k_{n_k}$  are the indices  $i$  for the flight conditions in family  $k$ , we will have

$$M_{k_1} = M_{k_2} = M_{k_{n_k}} \quad (5)$$

Then we extract a subset of the surface pressure database that consists of the entire surface pressure coefficient fields for these  $n_k$  solutions.

$$\mathbf{C}_k = [\mathbf{c}_{k_1} \quad \mathbf{c}_{k_2} \quad \cdots \quad \mathbf{c}_{k_{n_k}}] \quad (6)$$

At this stage, there is also the option to subtract the mean snapshot from each column before proceeding to the next step:

$$\bar{\mathbf{c}}_k = \frac{1}{n_k} \sum_{i=1}^{n_k} \mathbf{c}_{k_i} \quad \mathbf{C}_k = [\mathbf{c}_{k_1} - \bar{\mathbf{c}}_k \quad \mathbf{c}_{k_2} - \bar{\mathbf{c}}_k \quad \cdots \quad \mathbf{c}_{k_{n_k}} - \bar{\mathbf{c}}_k] \quad (7)$$

Whether (6) or (7) is used, the remaining steps are the same. In the examples shown in this paper, the mean-subtracted option following (7) is utilized.

We then compute a singular value decomposition of the  $n_x \times n_k$  matrix  $\mathbf{C}_k$

$$\mathbf{C}_k = \mathbf{\Phi} \mathbf{\Sigma} \mathbf{V}^T \quad (8)$$

The matrix  $\mathbf{\Phi}$  (note: this matrix is often written  $\mathbf{U}$ , but we are saving that letter of the alphabet for uncertainties, which will be discussed later) has column vectors that have the same dimension as the snapshot

surface pressure arrays.

$$\Phi = [\phi_1 \quad \phi_2 \quad \cdots \quad \phi_{n_k}] \quad \phi_i = \begin{bmatrix} \phi_{i,1} \\ \phi_{i,2} \\ \vdots \\ \phi_{i,n_x} \end{bmatrix} \quad (9)$$

The basis vectors also form an orthogonal matrix, so

$$\|\phi_i\|^2 = 1 \quad (10)$$

$$\phi_i \cdot \phi_j = \begin{cases} 1 & i = j \\ 0 & i \neq j \end{cases} \quad (11)$$

The matrix  $\Sigma$  is a rectangular matrix with so-called singular values along its diagonal.

$$\Sigma = \begin{bmatrix} \sigma_1 & 0 & \cdots & 0 \\ 0 & \sigma_2 & & 0 \\ \vdots & & \ddots & \vdots \\ 0 & 0 & \cdots & \sigma_{n_k} \\ 0 & 0 & \cdots & 0 \\ \vdots & \vdots & & \vdots \\ 0 & 0 & \cdots & 0 \end{bmatrix} \quad (12)$$

Finally, the matrix  $\mathbf{V}$  is defined so that the decomposition in (8) is satisfied. The singular values from (12) are a generalization of eigenvalues for rectangular matrices and are arranged in descending order such that

$$\sigma_1 \geq \sigma_2 \geq \dots \geq \sigma_{n_k} \geq 0$$

Each singular value  $\sigma_j$  is the  $L_2$  norm of norms when taking the dot product of the entire snapshot matrix  $\mathbf{C}_k$  with the mode  $\phi_j$ .<sup>4</sup> It is common to summarize this by saying  $\sigma_j$  describes how much “energy” of the snapshot matrix  $\mathbf{C}_k$  can be described by mode  $\phi_j$ . For example if all the snapshots are scale multiples of the first snapshot, then  $\sigma_1$  would have a nonzero value and  $\sigma_2$  and all the others would be zero.

Recall that each POD mode  $\phi_j$  has the same dimension as a surface pressure snapshot. Therefore the POD modes can be mapped back onto the original surface and plotted as a feature identification exercise and has been widely recognized for this property [20]. Figures 4 and 5 show two separate views of the first three modes at both Mach 0.5 and 1.75 for the Artemis I configuration of SLS from the 2017 FUN3D surface pressure database.

In Figures 4 and 5, a variant of the traditional blue-white-red surface pressure color scale is used: purple signifies a negative pressure coefficient (more precisely  $\phi_{i,j}$  value as described in (9)), white is close to zero, and orange is positive. This altered color scale is used throughout the paper to provide a visual identifier that a POD mode is shown rather than a nominal  $c_p$  solution.

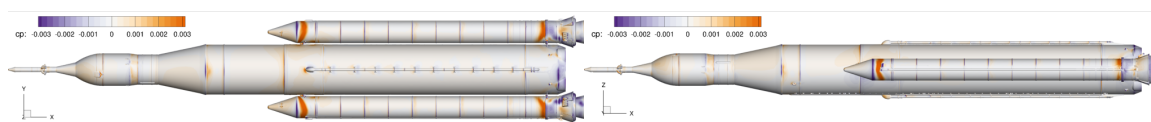
Furthermore, the bounds of the color bar are mostly irrelevant when plotting POD modes; because the root-sum-square of each  $\phi_i$  is by definition 1 (see (10)), a finer grid will have lower magnitudes for each entry, and vice versa. However, using a common scale (0.003 in Figures 4 and 5) shows how each POD mode either concentrates or spreads out its nonzero values.

It is common for the first few POD modes to have recognizable features and properties. For example, the first Mach 0.5 mode from Figure 4(a) has a negative normal force ( $C_N$ ) because the top surface is mostly purple ( $c_p < 0$ ) while the bottom (as seen from the left side view) is mostly orange ( $c_p > 0$ ). The second mode in Figure 4(b) has a similar nature but also includes significant but symmetric orange stripes near both the front and back of the boosters. Mode 3, as shown in Figure 4(c), has a significant net side force as the left side of the crew capsule near the front of the vehicle is orange while the right side is purple.

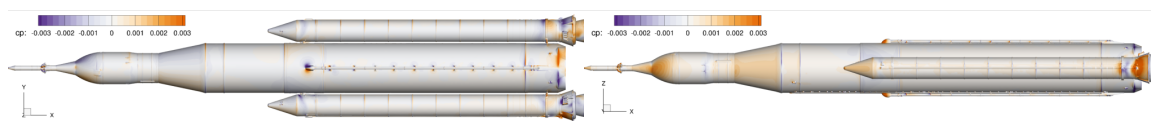
<sup>4</sup>This is an  $L_2$  norm in the vector sense; it does not account for triangles in the surface mesh with different areas, for example.



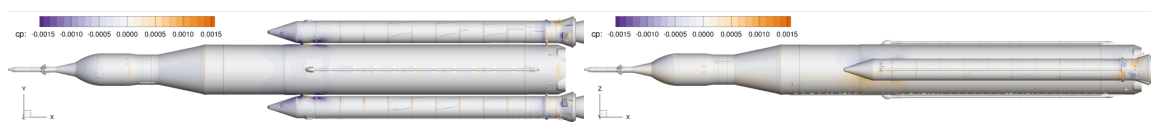
(a) Mach 0.50 mode 1, FUN3D



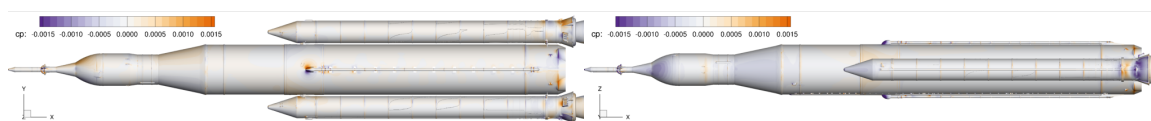
(b) Mach 0.50 mode 2, FUN3D



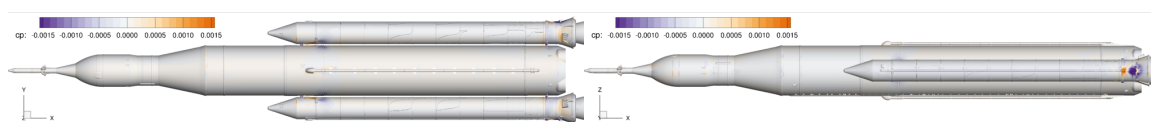
(c) Mach 0.50 mode 3, FUN3D



(d) Mach 0.50 mode 1, OVERFLOW



(e) Mach 0.50 mode 2, OVERFLOW



(f) Mach 0.50 mode 3, OVERFLOW

Figure 4: Top and left-side views of first 3 POD surface  $c_p$  modes at Mach 0.5

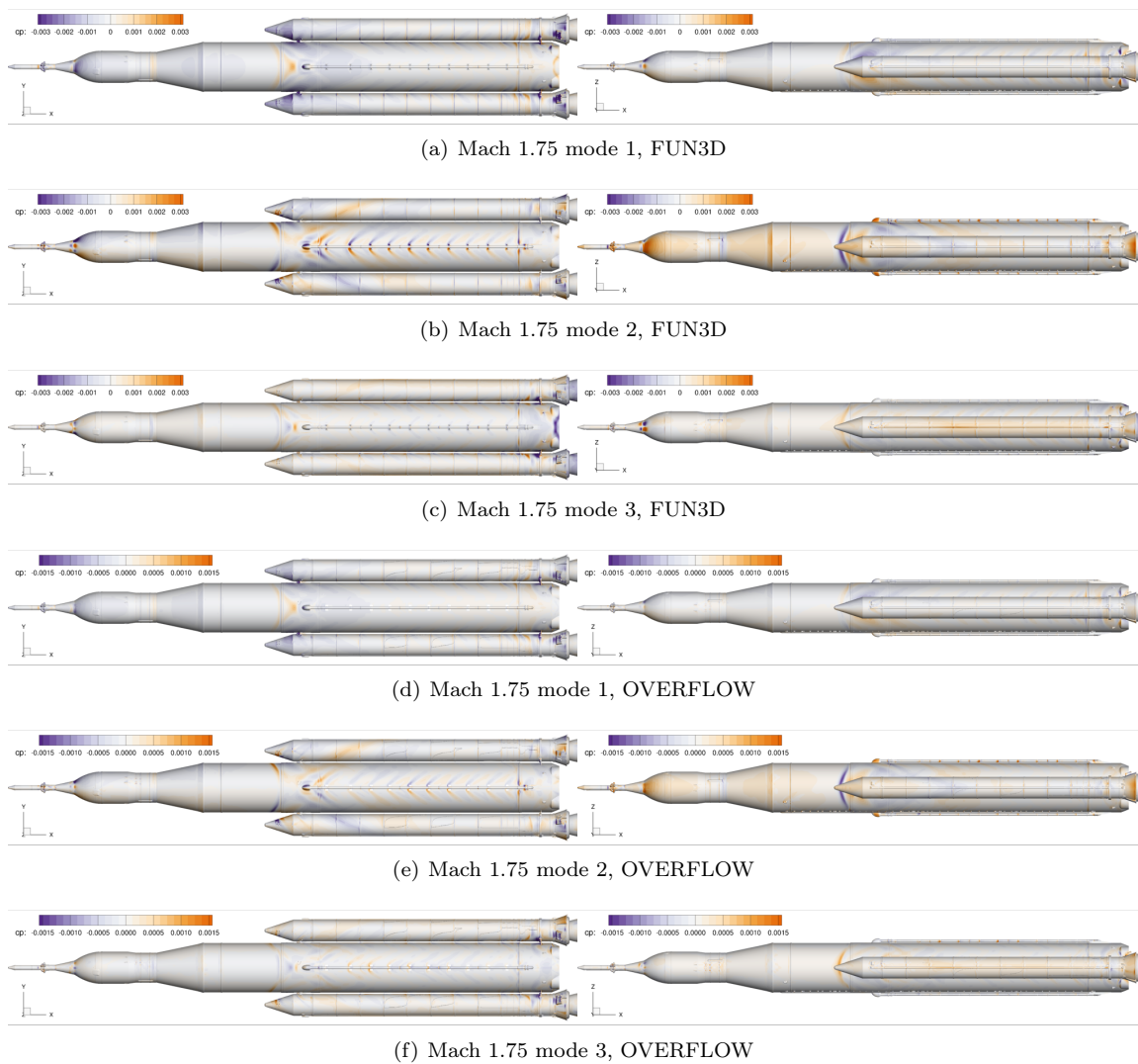


Figure 5: Top and left-side views of first 3 POD surface  $c_p$  modes at Mach 1.75

The first three modes from the OVERFLOW solutions at Mach 0.5 (Figures 4(d)-4(f)) show some but not all of the same features as the FUN3D (Figures 4(a)-4(c)). The main difference is actually that the ordering of the modes is not the same; OVERFLOW mode 2 is most similar to FUN3D mode 3 but with the sign reversed (which is arbitrary), and FUN3D mode 2 actually matches OVERFLOW mode 4. Ordering of the modes in this application is somewhat sensitive because the singular values decrease slowly (typically about 0.15 for the first mode and about 0.01 by the 20th mode). In addition, the OVERFLOW simulations did not include simulated rocket plumes, which leads to the OVERFLOW modes placing less emphasis on the aft portion of the vehicle.

Surface pressures typically have more sharp features at higher Mach numbers, and the POD modes are no different, as the Mach 1.75 example in Figure 5 shows. For example the top view of the second mode, shown in Figure 5(b), has easily identifiable shock structures along the top center of the back half of the vehicle. These are anchored to brackets that help support a liquid oxygen feed line that carries liquid oxygen from its tank near the top of main SLS stage around the large liquid hydrogen tank (instead of through it) and down to the engine section where it can be mixed with the hydrogen. Interestingly, these shock structures in Figure 5(b) are approximately antisymmetric, which would be unusual for a direct CFD surface pressure solution. Meanwhile, these same shocks are far less prominent in modes 1 and 3 (Figures 5(a) and 5(c)). The differences among these three modes provides an idea of how linear combinations of the same POD modes might be used to stably alter the six integrated forces and moments.

### 3.3 Surface Pressure Adjustment

A modified surface pressure distribution ( $c'_i$ ) for one flight condition  $\mathbf{r}_i = (M_i, \alpha_i, \beta_i)$  under this technique is constructed using the original CFD solution plus a linear combination of the POD modes:

$$\mathbf{c}'_i = \mathbf{c}_i + \sum_{j=1}^K a_j \phi_j \quad (13)$$

Here  $K \leq n_k$  is a subset of the full number of available POD modes. One typical approach to selecting  $K$  is to capture a pre-specified fraction of the singular values, i.e. select  $K$  such that

$$f = \frac{\sum_{j=1}^K \sigma_j}{\sum_{l=1}^{n_k} \sigma_l} \quad (14)$$

is at least 0.9 or some similar fraction. In the examples shown here,  $K=20$  and  $n_k=33$ .

The adjusted surface pressure distribution  $\mathbf{c}'_i$  from (13) must satisfy 6 constraints, one for each force and/or moment coefficient:

$$\begin{bmatrix} C_A \\ C_Y \\ C_N \end{bmatrix} = - \iint_S c'_i(x, y, z) \hat{\mathbf{n}} \, d\hat{A} \quad \begin{bmatrix} C_\ell \\ C_m \\ C_n \end{bmatrix} = \iint_S c'_i(x, y, z) (\hat{\mathbf{x}} - \hat{\mathbf{x}}_{MRP}) \times \hat{\mathbf{n}} \, d\hat{A} \quad (15)$$

where  $d\hat{A}$  is a small patch of the surface and  $\hat{A}=A/A_{ref}$  is just area normalized by a reference area. Also,  $\hat{\mathbf{n}}$  is the local unit surface normal (in most practical cases, of a surface grid triangle),  $\hat{\mathbf{x}}$  is the  $x, y, z$  coordinates of a point on the surface divided by a reference length  $L_{ref}$ , and  $\hat{\mathbf{x}}_{MRP}$  is the normalized location of the moment reference point. In other words, (15) states that the surface pressure must integrate to match the externally specified integrated forces & moments.

In practice, using (15) directly is impractical. Instead, the next step is to integrate the surface pressures for each of the  $K$  POD modes. For example

$$C_{A,j} = - \iint_S \phi_j \hat{\mathbf{n}} \cdot \hat{\mathbf{e}}_1 \, d\hat{A} \quad (16)$$

Once each mode has been integrated thusly, the six constraints on the adjusted surface can be rewritten

$$\begin{aligned}
 C_A &= C_A(\mathbf{c}_i) + \sum_{j=1}^K a_j C_{A,j} & C_\ell &= C_\ell(\mathbf{c}_i) + \sum_{j=1}^K a_j C_{\ell,j} \\
 C_Y &= C_Y(\mathbf{c}_i) + \sum_{j=1}^K a_j C_{Y,j} & C_m &= C_m(\mathbf{c}_i) + \sum_{j=1}^K a_j C_{m,j} \\
 C_N &= C_N(\mathbf{c}_i) + \sum_{j=1}^K a_j C_{N,j} & C_n &= C_n(\mathbf{c}_i) + \sum_{j=1}^K a_j C_{n,j}
 \end{aligned} \tag{17}$$

From (13), it is clear that the technique is linear, so instead of solving (17) for each case in the surface pressure database and/or each random draw of  $\varepsilon$  in (1), it is simpler to simply create a surface pressure profile that increases  $C_A$  by 1 but leaves the other five unchanged. Then the process is repeated to construct a mode that increases  $C_Y$  and leaves  $C_A$ ,  $C_N$ ,  $C_\ell$ ,  $C_m$ , and  $C_n$  unchanged, and so on.

The constraints for the surface pressure profile that increases  $C_A$  by 1 while leaving the other five unchanged is a special case of (17):

$$\begin{aligned}
 1 &= \sum_{j=1}^K a_j C_{A,j} & 0 &= \sum_{j=1}^K a_j C_{\ell,j} \\
 0 &= \sum_{j=1}^K a_j C_{Y,j} & 0 &= \sum_{j=1}^K a_j C_{m,j} \\
 0 &= \sum_{j=1}^K a_j C_{N,j} & 0 &= \sum_{j=1}^K a_j C_{n,j}
 \end{aligned}$$

A similar set of constraints exists for the  $C_Y$  mode, etc., simply by changing where the left-hand-side 1 occurs.

So now there are 6 constraints and  $K$  degrees of freedom; naturally an optimization approach is desired to solve for a single adjustment mode for each force or moment coefficient. In this work, as in [9], an objective function is selected that favors making the smallest possible adjustments to existing surface pressures. Specifically, the optimization problem is

$$\begin{aligned}
 \min_{\mathbf{a}} \in \mathbb{R}^K \quad f(\mathbf{a}) &= \sum_{j=1}^K w_j a_j^2 \\
 w_j &= |\phi_j|_\infty / \sigma_j
 \end{aligned} \tag{18}$$

Using the  $L$ -infinity norm in the weights  $w_j$  is an option that biases the optimization towards POD modes that spread out the nonzero signal. In other words it explicitly disfavors sharper, point-like modes. Currently this is a user-preference option as no method has been yet developed to decide if this improves results. Since the modes are already normalized to have an  $L_2$  norm of 1, it might be safe to simply use 1 for the numerator here.

Putting the singular value for mode  $j$ ,  $\sigma_j$  in the denominator is more concretely justifiable as it allows the optimization to favor modes that are more representative of the existing CFD surface pressure data. The singular value goes in the denominator so that modes with low singular values have a high weight  $w_j$ , which in turn causes the optimization to work hard to reduce the amount  $a_j$  of the mode used in the final adjustment mode.

In order to solve the minimization problem (18) subject to the constraints of (17), Lagrange multipliers

are used. Consider the Lagrangian

$$\begin{aligned}
 F(a_1, \dots, a_K, \lambda_1, \dots, \lambda_6) = & \sum_{j=1}^K w_j a_j^2 \\
 & + \left( \Delta C_A - \sum_{j=1}^K a_j C_{A,j} \right) \lambda_1 + \left( \Delta C_\ell - \sum_{j=1}^K a_j C_{\ell,j} \right) \lambda_4 \\
 & + \left( \Delta C_Y - \sum_{j=1}^K a_j C_{Y,j} \right) \lambda_2 + \left( \Delta C_m - \sum_{j=1}^K a_j C_{m,j} \right) \lambda_5 \\
 & + \left( \Delta C_N - \sum_{j=1}^K a_j C_{N,j} \right) \lambda_3 + \left( \Delta C_n - \sum_{j=1}^K a_j C_{n,j} \right) \lambda_6 \quad (19)
 \end{aligned}$$

To minimize the Lagrangian, set the derivative of  $F$  with respect to each  $a_j$  and  $\lambda$  equal to zero.

$$\frac{\partial F}{\partial a_j} = -\lambda_1 C_{A,j} - \lambda_2 C_{Y,j} - \lambda_3 C_{N,j} - \lambda_4 C_{\ell,j} - \lambda_5 C_{m,j} - \lambda_6 C_{n,j} + 2w_j a_j = 0 \quad (20)$$

This leads to a simple linear system of equations:

$$\begin{bmatrix}
 -2w_1 & 0 & \cdots & 0 & C_{A,1} & \cdots & C_{n,1} \\
 0 & -2w_2 & \ddots & \vdots & C_{A,2} & \cdots & C_{n,2} \\
 \vdots & \ddots & \ddots & 0 & \vdots & & \vdots \\
 0 & \cdots & 0 & -2w_K & C_{A,K} & \cdots & C_{n,K} \\
 C_{A,1} & C_{A,2} & \cdots & C_{A,K} & 0 & \cdots & 0 \\
 \vdots & \vdots & & \vdots & \vdots & \ddots & \vdots \\
 C_{n,1} & C_{n,2} & \cdots & C_{n,K} & 0 & \cdots & 0
 \end{bmatrix}
 \begin{bmatrix}
 a_1 \\
 a_2 \\
 \vdots \\
 a_K \\
 \lambda_1 \\
 \vdots \\
 \lambda_6
 \end{bmatrix}
 =
 \begin{bmatrix}
 0 \\
 0 \\
 \vdots \\
 0 \\
 \Delta C_A \\
 \vdots \\
 \Delta C_n
 \end{bmatrix} \quad (21)$$

In fact, the system is simple enough that it can be rewritten with six columns on the right-hand side so that all 6 adjustment modes can be attained with a single matrix solve. Denote the  $(K+6) \times (K+6)$  matrix on the left as  $\mathbf{A}$ , let  $\mathbf{a}_{C_A}$  be the vector of  $a$  coefficients for the  $C_A + 1$  mode, and let  $\boldsymbol{\lambda}_{C_A}$  be the corresponding Lagrange multipliers.

$$\mathbf{A} \begin{bmatrix} \mathbf{a}_{C_A} & \mathbf{a}_{C_Y} & \cdots & \mathbf{a}_{C_n} \\ \boldsymbol{\lambda}_{C_A} & \boldsymbol{\lambda}_{C_Y} & \cdots & \boldsymbol{\lambda}_{C_n} \end{bmatrix} = \begin{bmatrix} \mathbf{0}_{K \times 6} \\ \mathbf{I}_{6 \times 6} \end{bmatrix} \quad (22)$$

Here  $\mathbf{0}_{K \times 6}$  is a  $K \times 6$  matrix of zeros and  $\mathbf{I}_{6 \times 6}$  is the  $6 \times 6$  identity matrix.

The result of all this work is 6 surface pressure adjustment modes that can be added to the original surface pressure solution directly produced by CFD (or otherwise in the original database) to match target values of each integrated force and moment coefficient.

## 4 SLS Distributed Load Examples

Figures 6–9 show examples of the Mach 0.5, 0.95, and 1.75 surface pressure modes created using the previously described methods to alter each integrated force and moment coefficient for the Artemis I surface pressure created using FUN3D and OVERFLOW. A modified green-white-brown color map is used for the adjustment modes to provide a visual signal that these are not surface pressures at any particular flight condition (blue-red) or POD modes (purple-orange). Green values represent decreases in pressure coefficient, and brown values represent increases.

On the left-hand side of each row of figures is a top view of SLS, and on the right is a view of the bottom side but with the direction of flight reversed. This flipped view keeps the right booster on the top for both

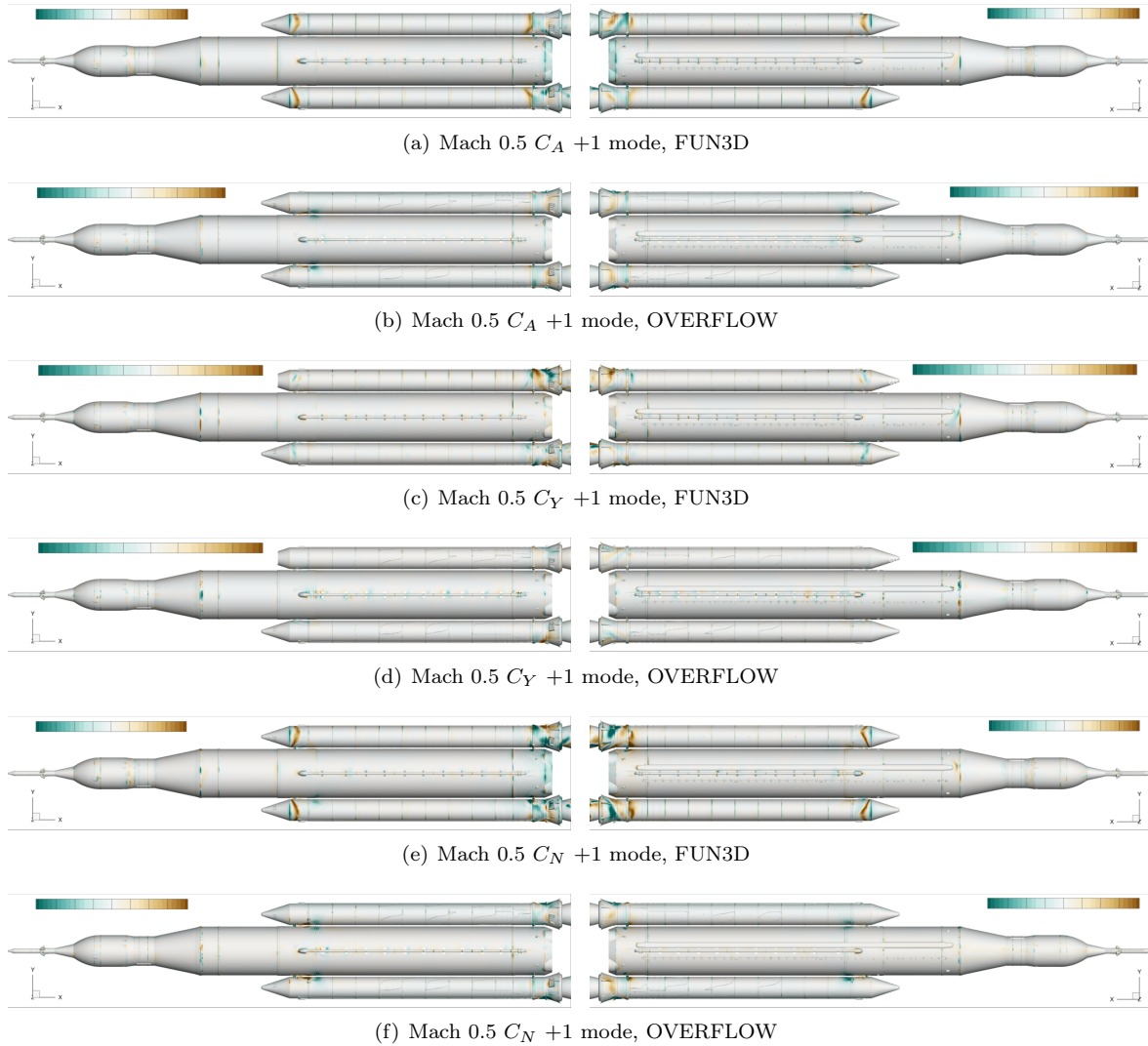


Figure 6: Force coefficient adjustment surface  $\Delta c_p$  profiles for Mach 0.5

images and the left booster on the bottom, so symmetry is easier to assess visually.

For example, the suggested method to increase  $C_A$  at Mach 1.75, shown in Figure 8(a), is to decrease the pressure on the SRB nozzles and base of the SRB “skirt”<sup>5</sup>. The lateral modes,  $C_Y$ ,  $C_\ell$ , and  $C_n$  in Figures 8(c), 9(a), and 9(e), respectively, have noticeable antisymmetry between the left and right sides. Meanwhile the two longitudinal modes,  $C_N$  and  $C_m$  in Figures 8(e) and 9(c), are roughly left-right symmetric.

These modes have many other notable features for an engineer who is tasked to use surface pressures for a downstream purpose.

- Near the top of the vehicle there are four abort motor nozzles that are not aligned with either the  $y$  or  $z$  axes. Downstream of these nozzles is a cone section that transitions into an ogive. At this transition, each image in Figure 8 has a significant signal, which can be either checkerboard or stripes.
- The largest conical section, called the Launch Vehicle Stage Adapter, or LVSA, has very little brown or green on it for any mode. This suggests the CFD is highly confident in the loads on this section

<sup>5</sup>In the SLS Program, the contributions of this region to  $C_A$  are accounted for in a separate database since the plume effects are significant here; however the contributions of this region to the other 5 coefficients are accounted for in the external aerodynamic database. For this paper, those complexities are neglected to avoid lengthy discussions that would distract from the main point of the paper.

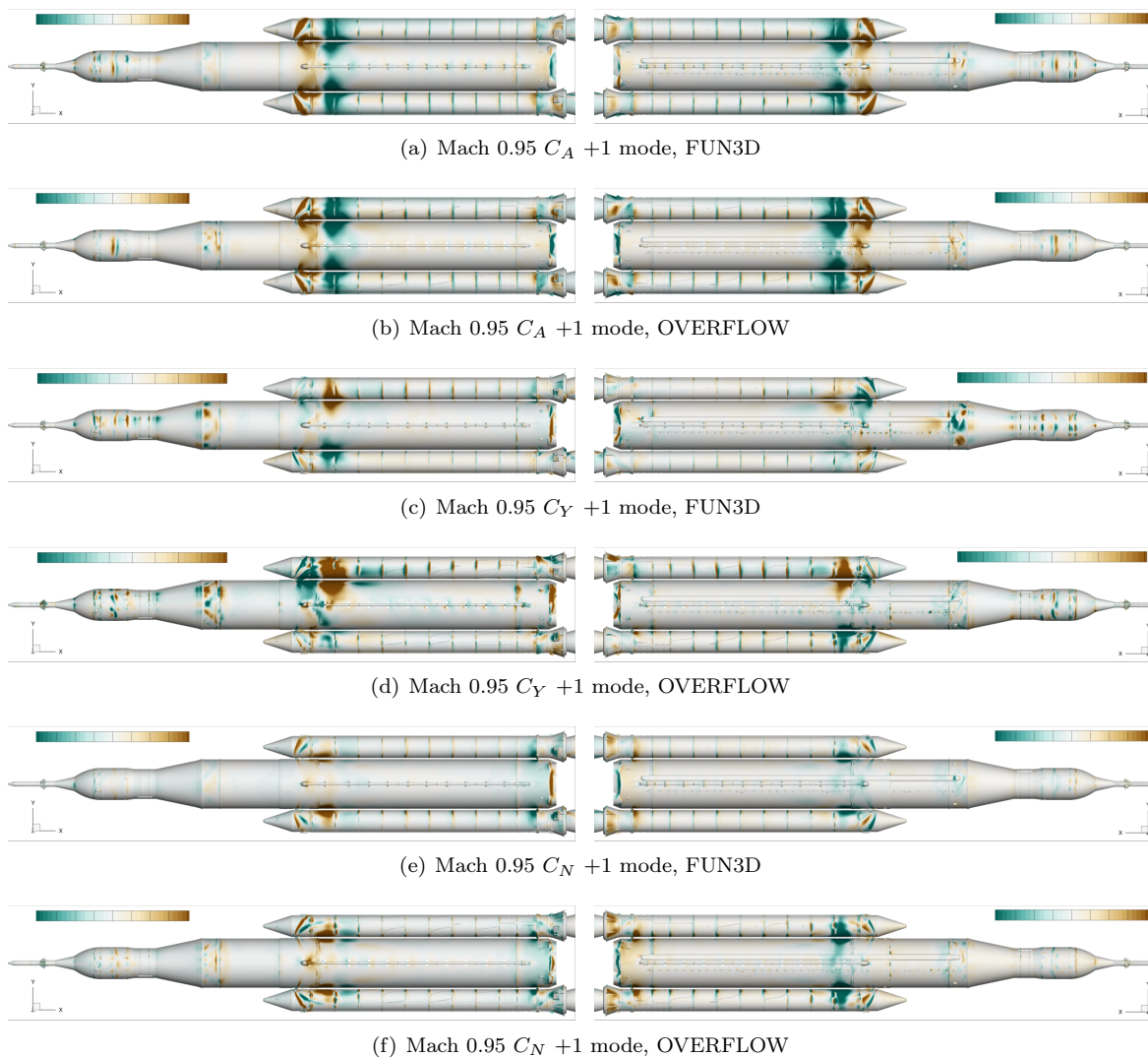


Figure 7: Force coefficient adjustment surface  $\Delta c_p$  profiles for Mach 0.95

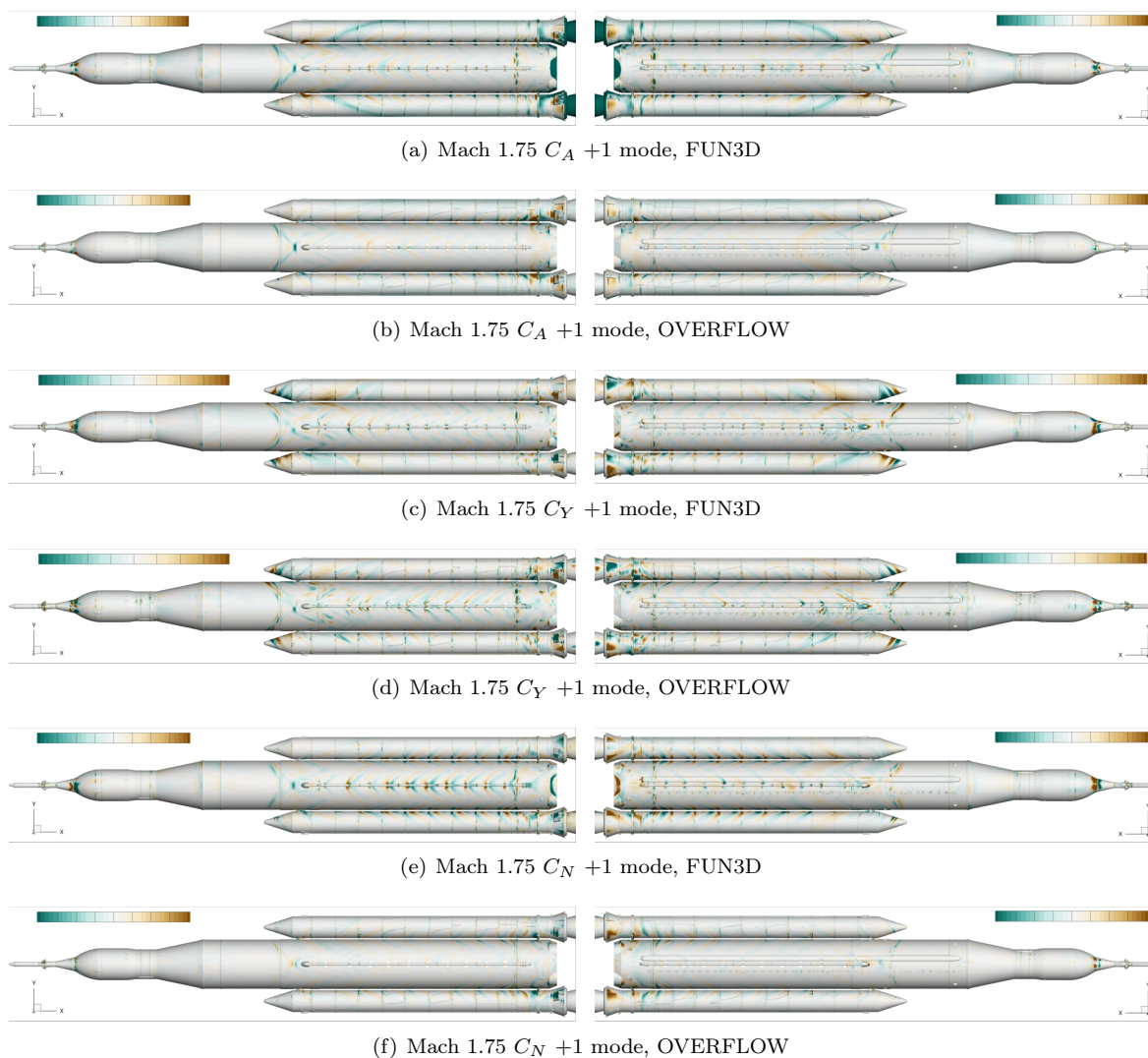
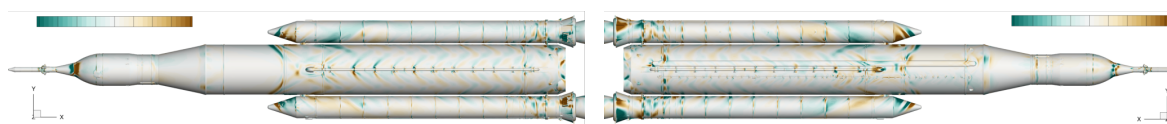
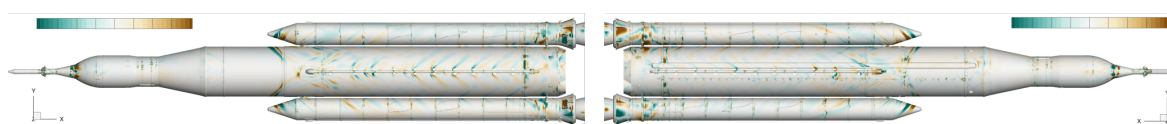


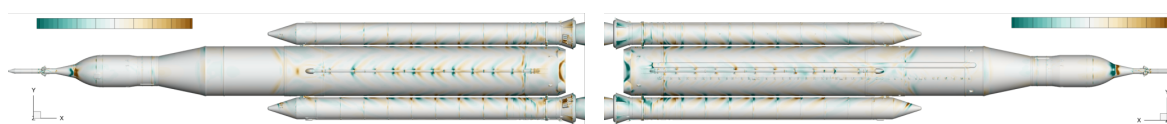
Figure 8: Force coefficient adjustment surface  $\Delta c_p$  profiles for Mach 1.75



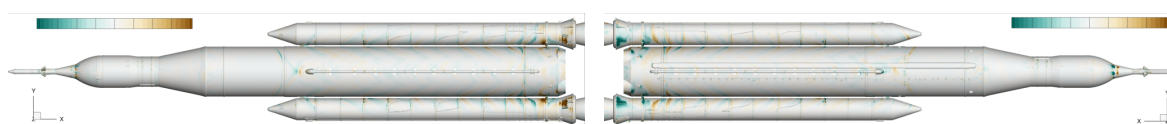
(a) Mach 1.75  $C_\ell$  +1 mode, FUN3D



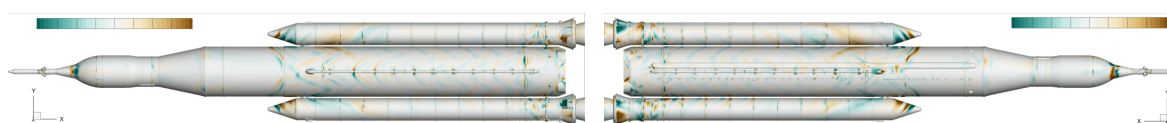
(b) Mach 1.75  $C_\ell$  +1 mode, OVERFLOW



(c) Mach 1.75  $C_m$  +1 mode, FUN3D



(d) Mach 1.75  $C_m$  +1 mode, OVERFLOW



(e) Mach 1.75  $C_n$  +1 mode, FUN3D



(f) Mach 1.75  $C_n$  +1 mode, OVERFLOW

Figure 9: Moment coefficient adjustment surface  $\Delta c_p$  profiles for Mach 1.75

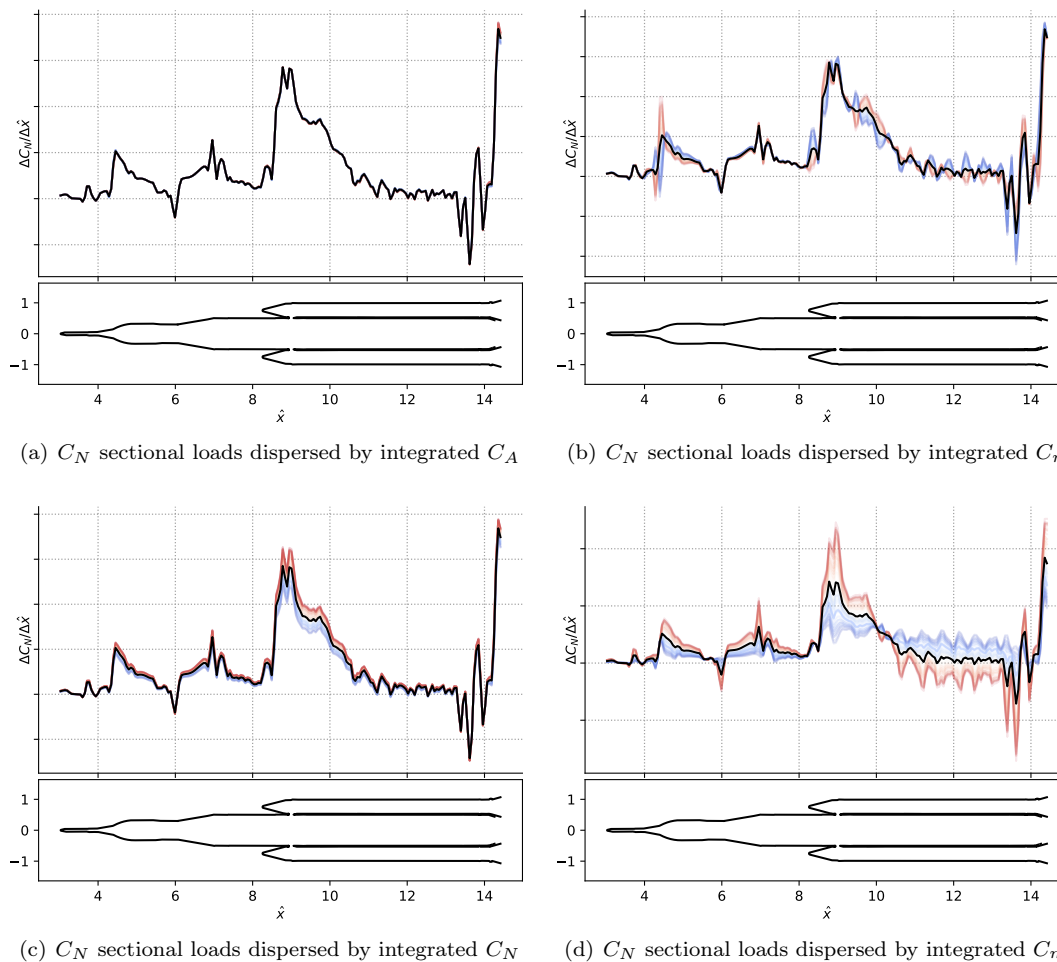


Figure 10: Dispersed normal sectional loads from FUN3D at Mach 1.75,  $4^\circ$  angle of attack and  $0^\circ$  sideslip. Red curves correspond to an increase in the integrated coefficient while blue curves correspond to a decrease.

even though those are some of the most significant loads on the vehicle.

- The area around the noses of the left and right boosters seem to have the most brown and green area.
- The  $C_\ell$  mode in Figure 9(a) has left-right antisymmetry on the entire boosters but top-bottom antisymmetry only near the back of the boosters; this is likely an artifact of keeping  $C_m$  and  $C_n$  constant.
- The Mach 0.5 modes (Figure 6) mostly suggest changes to the pressures around the front and back of the boosters, while the supersonic modes have changes to the surface pressure over more of the vehicle.
- Mach 0.95 adjustment modes (Figure 7) mostly suggest changes to the area near the forward attach hardware, just downstream of the booster noses.

As an example of utilization of the dispersed surface pressures, Figure 10 shows the sectional loads (line loads) in the vertical direction ( $C_N$ ) for a critical flight condition where SLS is expected to encounter the maximum longitudinal loads. This flight condition is Mach 1.75 with  $4^\circ$  angle of attack and  $0^\circ$  sideslip angle. For SLS Mach 1.75 is the point during ascent with the maximum dynamic pressure, and  $4^\circ$  is the total angle of attack limit. There three sectional loads for each flight condition,  $C_A$ ,  $C_Y$ , and  $C_N$ . In Figure 10, only the  $C_N$  loads are shown, but the effects of dispersions in four of the six integrated force & moment coefficients are shown.

The integrated force & moment uncertainty quantification implementation has six separate magnitudes, and each has its own independent random variable.

$$\begin{aligned}
 \tilde{C}_A &= C_A + \varepsilon_{CA} U_{CA} & \tilde{C}_\ell &= C_\ell + \varepsilon_{C\ell} U_{C\ell} \\
 \tilde{C}_Y &= C_Y + \varepsilon_{CY} U_{CY} & \tilde{C}_n &= C_n + \varepsilon_{Cn} U_{Cn} + (\hat{x}_{MRP} - \hat{x}_{cg}) \varepsilon_{CY} U_{CY} \\
 \tilde{C}_N &= C_N + \varepsilon_{CN} U_{CN} & \tilde{C}_m &= C_m + \varepsilon_{Cm} U_{Cm} + (\hat{x}_{MRP} - \hat{x}_{cg}) \varepsilon_{CN} U_{CN}
 \end{aligned} \tag{23}$$

The extra terms involving the moment reference point and the center of gravity ( $\hat{x}_{cg}$ ) in (23) just make it so that  $\varepsilon_{Cm} U_{Cm}$  is the dispersion in the pitching moment about the center of gravity, even though  $C_m$  and  $\tilde{C}_m$  are moments about the fixed moment reference point [6]. In Figure 10, the black curve is the original longitudinal ( $C_N$ ) line load for Mach 1.75, which includes the skin friction and is not consistent with the integrated loads from the wind tunnel. Each blue or red curve represents a  $C_N$  line load constructed by

1. first picking one value of one  $\varepsilon$  value from (23) and holding the others at 0,
2. applying a surface pressure change consistent with that epsilon value, e.g.  $\varepsilon_{CN} U_{CN}$ .
3. calculating the line load associated with that  $c_p$  change using the `triload` tool [21], from Chimera Grid Tools[22, 23], and
4. adding that to the black curve.

The magnitudes for  $U_{CA}$ ,  $U_{Cn}$ , etc. are the current values from the Artemis I flight database. In each case, the  $\varepsilon$  value is randomly drawn assuming a uniform distribution on  $[-1, 1]$ , and the curve is blue if  $\varepsilon = -1$ , gray if  $\varepsilon = 0$ , red if  $\varepsilon = 1$ , and varying continuously in between. The numbers have been removed from the  $y$ -axis because these data are export restricted.

Figure 10(a) shows the effect on the  $C_N$  sectional loads caused by a change in the integrated  $C_A$ , or force coefficient parallel with the centerline of the vehicle. In this case, the line loads show little dispersion, meaning that pressure changes selected to alter  $C_A$  were relatively symmetric and do not cause significant changes to any section's net  $C_N$ .

Figure 10(b) shows the effect of dispersing integrated  $C_n$  on the same  $C_N$  sectional loads. In this case, there is a significant effect, which means that the surface pressure modes were unable to alter the lateral loads without spilling over into the longitudinal loads. The most significant blue/red spike appears to be near the nose of the vehicle where the conical section meets the ogive. As mentioned previously, wakes from the launch abort motor nozzles are present here. Furthermore, the abort nozzles are not aligned with the vehicle's  $y$  and  $z$  axes, so changes to the local pressure that target  $C_Y$  or  $C_n$  are likely to also affect  $C_N$  and  $C_m$ . Cross-correlated sectional loads such as this example are not possible using a similar approach that only disperses sectional loads directly as described in [9].

Figures 10(c) and 10(d) show the direct effects of dispersing the integrated  $C_N$  and  $C_m$  on the distributed  $C_N$  sectional loads. The effects of  $\varepsilon_{CN}$  are relatively proportional to the nominal black  $C_N$  sectional load curve, though not exactly. In Figure 10(d), the approximate center of gravity,  $\hat{x}_{cg}$  is readily visible because the red and blue flip at around  $\hat{x}_{cg} = 10$ .

## 5 Extensions and Limitations

Several extensions to the surface pressure adjustment techniques developed in Section 3 are interesting and do not add any appreciable mathematical complexity.

1. The viscous contributions to loads could be considered by including the three components of the skin friction coefficient to the snapshots in (3) and (6).
2. Additional constraints can be added such as specifying directly the desired pressure coefficient at one or more points on the surface.
3. Results from CFD on finer grids, different geometry, different conditions, etc. can be added to provide the opportunity for direct CFD uncertainty quantification.

4. The approach can be extended to the entire flow solution instead of just the surface.

First consider the addition of the viscous contributions when constructing and modifying the distributed loads. Compared to the techniques described in Section 3.2, the snapshots grow by a factor of 4: instead of just the surface pressure coefficient ( $c_p$ ) at each point on the surface, the snapshot now must include the three components of the skin friction coefficient ( $c_{f_x}, c_{f_y}, c_{f_z}$ ). Then the methods in Section 3.3 proceed unmodified except that (16) and its five unwritten siblings must also include the viscous contributions when calculating the forces & moments on each POD mode. The liftoff & transition work in [10] is one example where the skin friction was modified along with the surface pressure in roughly this fashion. For SLS ascent, the viscous contributions to overall forces & moments are generally quite small, but the main reason they were not included in the preceding sections is that SLS maintains an official surface pressure database but not a skin friction database.

The next extension to consider would be to impose additional constraints on the adjusted surface pressure profiles. In general each additional constraint will add one column and one row (and one Lagrange multiplier) to the matrix equation in (21). One relatively straightforward extension would be to impose forces and moments on subcomponents, for example the left and right boosters and the remaining centerbody. In this example there could be up to 18 constraints if all six coefficients are constrained separately for three components.

Another additional constraint to consider is to specify the surface pressure match a specific value at a specific point. The motivation for this idea is a wind tunnel experiment that is instrumented with one or more surface pressure taps. Following the same approach as described in Section 3.3, it is possible to construct a mode that is a linear combination of the POD modes that adjusts the pressure at one tap location while leaving the integrated forces & moments unchanged. To do this we add another row (and) column to the matrix in (21) that evaluates each POD mode at the location of that tap. So if for example there is a pressure tap at  $(x_{P1}, y_{P1}, z_{P1})$ , and  $c_{p,j,P1}$  is the pressure coefficient of POD mode  $j$  at location  $P1$ , then the system of equations becomes

$$\begin{bmatrix} -2w_1 & 0 & \cdots & 0 & C_{A,1} & \cdots & C_{n,1} & c_{p,1,P1} \\ 0 & -2w_2 & \ddots & \vdots & C_{A,2} & \cdots & C_{n,2} & c_{p,2,P1} \\ \vdots & \ddots & \ddots & 0 & \vdots & & \vdots & \vdots \\ 0 & \cdots & 0 & -2w_K & C_{A,K} & \cdots & C_{n,K} & c_{p,K,P1} \\ C_{A,1} & C_{A,2} & \cdots & C_{A,K} & 0 & \cdots & 0 & 0 \\ \vdots & \vdots & & \vdots & \vdots & \ddots & \vdots & \vdots \\ C_{n,1} & C_{n,2} & \cdots & C_{n,K} & 0 & \cdots & 0 & 0 \\ c_{p,1,P1} & c_{p,2,P1} & \cdots & c_{p,K,P1} & 0 & \cdots & 0 & 0 \end{bmatrix} \begin{bmatrix} a_1 \\ a_2 \\ \vdots \\ a_K \\ \lambda_1 \\ \vdots \\ \lambda_6 \\ \lambda_7 \end{bmatrix} = \begin{bmatrix} 0 \\ 0 \\ \vdots \\ 0 \\ \Delta C_A \\ \vdots \\ \Delta C_n \\ \Delta c_{p,P1} \end{bmatrix} \quad (24)$$

While relatively interesting in that it allows an engineer to construct surface pressures that match experimental measurements exactly, it introduces several risks:

- With many pressure taps to match, the appropriate number of POD modes to use may become excessive
- If the CFD is highly confident about the pressure at a given location, but it differs from the experimental measurement, the results may be unstable, for example imposing large  $c_p$  changes far away from the pressure tap
- Even if those problems are avoided, the resulting pressure distribution to modify  $c_p$  at one point will likely change the pressure over much of the vehicle to avoid changes to the integrated loads

In practice this extension is not recommended because it overconstrains the pressure distribution where the CFD, if run using best practices, already provides the best estimate.

Some of the above issues can be mitigated by localizing the POD modes, for example by multiplying each POD mode by a mask that is 1 at  $P1$  and then decreases to 0 as a Gaussian function of spatial distance from  $P1$ . It is possible then, to construct surface pressure profiles that increase  $c_p$  at  $P1$  by 1, have no effect on integrated forces & moments, and are local to  $P1$ . Still, whether using (24) directly or this modified approach, modifying the pressure profile to match specific point pressures is hazardous. The main reason

the discussion is included here is to describe how additional constraints can be incorporated. In most cases, integral constraints are more appropriate than point-like constraints.

As currently described, the methods in Section 3 do not constitute an uncertainty quantification of distributed loads. It does perform a related task, which is to allocate uncertainty in integrated loads across the entire surface or into other distributed loads. In order to promote this technique to a direct uncertainty quantification of distributed loads, dedicated runs on a finer grid or with different values of other epistemic or aleatory variables would be needed, for example following approaches described in [13]. However, the techniques described here are still relevant; simply knowing the probability distribution of the  $c_p$  at each point is not sufficient because the correlation between dispersions at each point is still needed. In other words, the techniques described here can turn knowledge about the uncertainty at each point into global surface modes.

As far as including the entire flow solution instead of just the surface, POD of volume solutions has certainly been performed [8]. One example where such information could be useful is boundary layer profiles at key locations, for example at vents on the SLS vehicle where internal some internal compartments must vent their sea-level air as the vehicle ascends through the atmosphere.

## 6 Conclusion and Future Work

A generic method to adjust distributed aerodynamic loads to match either wind-tunnel integrated loads or an external uncertainty quantification of integrated loads has been developed and applied to a surface pressure database for the Artemis I launch vehicle. Specifically, the methods adjust the surface pressure from a best-practices CFD solution to match a full 3D set of integrated forces and moments from wind tunnel test and then repeat the procedure for any point within the uncertainty bounds of that wind tunnel-based force & moment database.

The methods have been applied to databases from the Space Launch System Program for the first three flights of the Artemis Program to demonstrate their applicability to actual large-scale engineering problems. Results have been shown for solutions from two different leading Navier-Stokes CFD solvers from NASA: FUN3D and OVERFLOW. With the assumption of a large database of available CFD solutions, as is the case for SLS, the techniques developed here do not require any additional CFD solutions to enable the uncertainty distribution capability. Finally, the adjusted surface pressures have been mapped to 1D sectional loads to demonstrate the ability of this method to inform structural analysts; guidance, navigation, & control teams; etc. of the impact from integrated force & moment uncertainty on any quantity that can be derived from surface pressures.

The paper describes several extensions, such as also adjusting the surface pressure at one or more discrete points, that can be implemented by the reader. Future work includes combining the technique with dedicated CFD uncertainty quantification. Additional advances may include techniques for improved quality control and more rigorous approaches to the objective function used to optimize pressure adjustment profiles.

## Acknowledgments

Resources supporting this work were provided by the NASA High-End Computing Capability (HECC) program through the NASA Advanced Supercomputing (NAS) Division at Ames Research Center. This work was funded by the Space Launch System (SLS) Program.

## References

- [1] Space Launch System. <https://www.nasa.gov/exploration/systems/sls/index.html>.
- [2] Apollo 17 Command and Service Module (CSM). <https://nssdc.gsfc.nasa.gov/nmc/spacecraft/display.action?id=1972-096A>. NSSDCA/COSPAR ID: 1972-096A.
- [3] Orion Spacecraft. <https://www.nasa.gov/exploration/systems/orion/index.html>.
- [4] Exploration Ground Systems. <https://www.nasa.gov/exploration/systems/ground/index.html>.
- [5] Gateway. <https://www.nasa.gov/gateway>.

- [6] A. Favaregh, H. Houlden, and J. Pinier. Space Launch System Aerodynamic Database Uncertainty Quantification Methodologies. In *54th AIAA Aerospace Sciences Meeting*, 2016. AIAA Paper 2016-0795.
- [7] Stuart E. Rogers, Derek J. Dalle, and William M. Chan. CFD Simulations of the Space Launch System Ascent Aerodynamics and Booster Separation. In *53rd AIAA Aerospace Sciences Meeting*, 2015. AIAA Paper 2015-0778.
- [8] Kenneth C. Hall, Jeffrey P. Thomas, and Earl H. Dowell. Proper orthogonal decomposition technique for transonic unsteady aerodynamic flows. *AIAA Journal*, 38(10):1853–1862, 2000.
- [9] D. Dalle, S. Rogers, and H. Leeand J. Meeroff. Adjustments and Uncertainty Quantification for SLS Aerodynamic Sectional Loads. In *2018 Applied Aerodynamics Conference*, 2018. AIAA Paper 2018-3640.
- [10] T.J. Wignall. Liftoff and Transition Database Generation for Launch Vehicles Using Data Fusion Based Modeling. In *AIAA Scitech 2019 Forum*, 2019. AIAA Paper 2019-1842.
- [11] R. T. Biedron, J. Carlson, J. M. Derlaga, P. A. Gnoffo, D. P. Hammond, W. T. Jones, E. M. Lee-Rausch, E. J. Nielson, M. A. Park, C. L. Rumsey, J. L. Thomas, and W. A. Wood. Fun3d manual: 13.1. Technical Report TM-2017-219580, NASA, 2017.
- [12] R. H. Nichols, R. W. Tramel, and P. G. Buning. Solver and Turbulence Model Upgrades to OVERFLOW2 for Unsteady and High-Speed Applications. In *36th AIAA Fluid Dynamics Conference*, 2006. AIAA Paper 2006-2824.
- [13] Tim Barth. An Overview of Combined Uncertainty and A-Posteriori Error Bound Estimates for CFD Calculations. In *54th AIAA Aerospace Sciences Meeting*, 2016. AIAA Paper 2016-1062.
- [14] P. R. Spalart and S. R. Allmaras. One-equation turbulence model for aerodynamic flows. *La Recherche Aeronautique*, 1(1):5–21, 1994.
- [15] AFLR3 Unstructured Grid Generator. <https://www.simcenter.msstate.edu/software/documentation/aflr3/index.html>.
- [16] Pieter G. Buning and Thomas H. Pulliam. Cartesian off-body grid adaption for viscous time-accurate flow simulations. In *20th AIAA Computational Fluid Dynamics Conference*, 2011. AIAA Paper 2011-3693.
- [17] Marian Nemec, Michael J. Aftomis, and Liam Smith. Uncertainty Estimates for Sonic-Boom Pressure Signatures and Loudness Carpets. In *AIAA AVIATION 2021 Forum*, 2021. AIAA Paper 2021-2753.
- [18] Christoph Brehm, Emre Sozer, Shayan Moini-Yekta, Jeffrey A. Housman, Michael F. Barad, Cetin C. Kiris, Bruce T. Vu, and Christopher R. Parlier. Computational prediction of pressure environment in the flame trench. In *31st AIAA Applied Aerodynamics Conference*, 2013. AIAA Paper 2013-2538.
- [19] Christoph Brehm, Jeffrey A. Housman, Cetin C. Kiris, and Florence V. Hutcheson. Noise characteristics of a four-jet impingement device inside a broadband engine noise simulator. In *21st AIAA/CEAS Aeroacoustics Conference*, 2015. AIAA Paper 2015-2211.
- [20] Scott M. Murman and Laslo T. Diosady. Simulation of a hammerhead payload fairing in the transonic regime. In *54th AIAA Aerospace Sciences Meeting*, 2016. AIAA Paper 2016-1548.
- [21] Shishir Pandya and William M. Chan. Computation of sectional loads from surface triangulation and flow data. In *20th AIAA Computational Fluid Dynamics Conference*, 2011. AIAA Paper 2011-3680.
- [22] W. M. Chan. The overgrid interface for computational simulations on overset grids. In *32nd AIAA Fluid Dynamics Conference*, June 2002. AIAA Paper 2002-3188.
- [23] S. E. Rogers, K. Roth, S. M. Nash, M. D. Baker, Slotnick J. P., M. Whitlock, and H. V. Cao. Advances in overset cfd processes applied to subsonic high-lift aircraft. In *18th AIAA Applied Aerodynamics Conference*, June 2000. AIAA Paper 2000-4216.